Research Article

Monalisa Halder* and Ajit Kumar Meikap

Dielectric relaxation and current conduction mechanism of Tb and Mn codoped bismuth ferrite grafted poly (vinyl alcohol) nanocomposite film

https://doi.org/10.1515/rams-2020-0040
Received Oct 29, 2019; accepted Apr 23, 2020

Abstract: Investigation on current conduction mechanism through Tb and Mn codoped Bismuth Ferrite grafted polyvinyl alcohol (BTFMO-PVA) nanocomposite film above room temperature (300 K – 415 K) is reported here in detail. A detailed study on dielectric properties of the sample is done over a wide temperature range in a frequency range of 20 Hz - 2 MHz. The conduction is attributed to correlated barrier hopping model. Bipolaron hopping dominates over single-polaron hopping in this system. Complex electric modulus spectra and complex modulus spectra are well explained by suitable models to understand the effective dielectric response. The sample responds to the externally applied magnetic field exhibiting negative magnetocapacitance at room temperature.

Keywords: nanocomposite film, charge conduction mechanism, dielectric response, magnetocapacitance

1 Introduction

Research on the development and the characterization of polymer composites with ferro-, pyro-, piezo-electric properties are very much in trend for showing unique electromagnetic responses [1]. The inclusion of nano-sized fillers in a polymer matrix element can enhance the multifunctional properties of the host polymer. A proper combination of nanofiller and polymer improves the physical, optical, electrical, and magnetic properties [2]. For the enhancement in the charge conduction mechanism of the polymer nanocomposite system, semiconductor type materials are generally used. Due to the accumulation of charge at the grain boundaries, interfacial polarisation plays a role in controlling the charge conduction mechanism of the composite system. Under suitable conditions, nanocomposite films prepared by drop-casting or sol-gel processes show better molecular interaction between the nanofiller and the polymer [3]. Out of many polymers, polyvinyl alcohol (PVA) is a widely used matrix element due to its non-toxicity, significant electrical properties, flexibility, reasonable tensile strength, and functional charge storage capacity [4]. In this work, we have focused on multiferroic-polymer nanocomposite. Recently many researchers are going on with this type of composite due to its multifunctionalities [5]. The dielectric/magneto-dielectric response, charge conduction mechanism in the polymer matrix can be significantly affected by the insertion of multiferroic nanofiller. In our previous work, we have discussed the current conduction mechanism of $BiFeO_3$ (BFO) nanofiller inserted PVA nanocomposite film [6]. Enhancement in current conduction was achieved in BFO-PVA film than the pristine PVA film. Bismuth Ferrite is a very relevant multiferroic as it simultaneously exhibits ferroelectric and antiferromagnetic properties at room temperature [7]. Here, Tb and Mn codoped $BiFeO_3$ (BTFMO) nanoparticles are dispersed in PVA matrix. Enhancement of electrical, magnetic properties has been reported with the doping of other ions at A or B site of Bismuth ferrite [7]. Meanwhile, the space charge polarisation induced by the dopants can act as additional dipoles [8].

The present article reports the charge conduction mechanism and dielectric relaxation, magneto-dielectric response, the interfacial polarisation of the film sample in the temperature range between 300 K to 415 K. Here, frequency-dependent electrical modulus spectroscopy, complex admittance spectroscopy, and complex impedance spectroscopy of the sample are studied to get the idea about the charge conduction mechanism through the materials. Variation of current with the application of voltage is also considered. These spectroscopic studies of

***Corresponding Author: Monalisa Halder:** Department of Physics, National Institute of Technology, Durgapur-713209, India;
Email: monalisahldr18@gmail.com; Tel.: +91 9434897414; Fax: +91 343 2547375
Ajit Kumar Meikap: Department of Physics, National Institute of Technology, Durgapur-713209, India

the conduction mechanism is first time reported for the present nanocomposite film.

2 Experimental Details

2.0 wt% of BTFMO ($Bi_{0.95}Tb_{0.05}Fe_{0.95}Mn_{0.05}O_3$) nanofillers are grafted in prepared polyvinyl alcohol (PVA) solution. DI water is taken as a solvent for PVA solution. By the drop-casting method, the solvent is evenly poured on a clean glass petri dish at room temperature. After natural drying for 7 days, the thin nanocomposite film is achieved by detaching it from the substrate (petri dish). For achieving a thin uniform film thickness (< 100 μm), little amount (15 ml) of BTFMO-PVA solution is poured on an even surface. In the present work, the wet film thickness was ~ 600 μm which produced 95 μm thick dry thin film (measured from FESEM image). The detailed experimental procedure is reported earlier [9].

The film sample is morphologically examined usinf field emission scanning electron microscopy (ZEISS EVO-MA 10). Before testing, the sample is coated with a thin layer of gold to avoid the electrical charging during the examination. Here, the current conduction mechanism of the film is studied elaborately in the temperature range 300 K – 415 K. For measuring the electrical properties, a parallel plate configuration is prepared by pasting silver (Acheson Colloiden B. V Holland) electrodes on both sides of a small square portion (average thickness 0.095±0.001 mm and area 10×10 mm^2) of the film sample. The temperature-dependent AC electrical measurements and dielectric response are studied in the frequency range 20 Hz – 2 MHz with Agilent E 4980A precision LCR meter using a furnace fitted with 8502 Eurotherm temperature controller cryostat in temperature range 300 K – 415 K. Room temperature magneto-dielectric response is measured using an electromagnet (EM-250). The current-voltage (I-V) characteristics are measured with a two-probe system of Keithley 2450 source measure unit (SMU) equipped with KickStart software.

3 Results and Discussions

The digital image of the thin nanocomposite film is given in Figure 1 (a). FESEM offers the topographical informations of the nanocomposite film at different magnifications with essentially unlimited depth of field. The thin film thickness is found to be ~ 95 μm from the cross-sectional image [inset of Figure 1 (c)]. The FESEM micrograph is

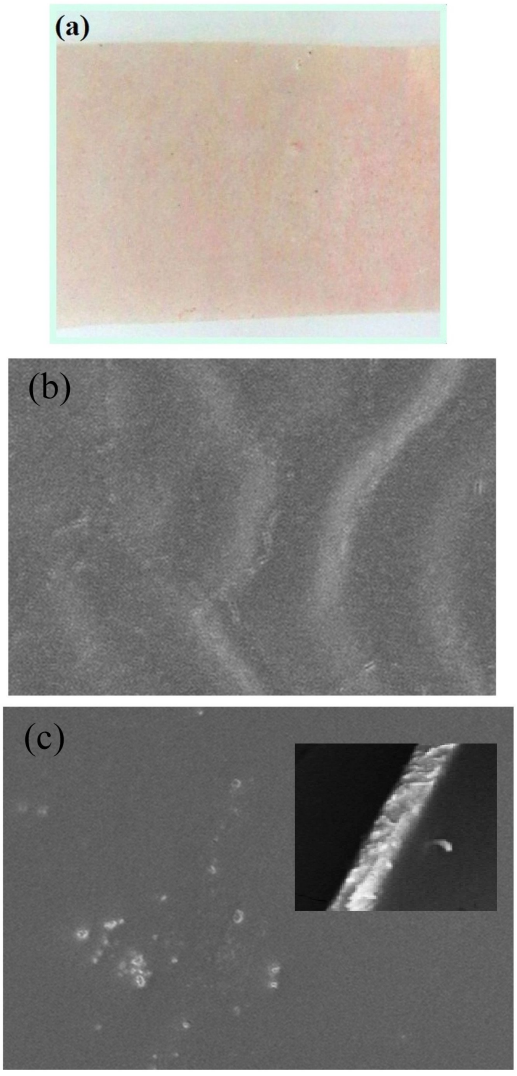

Figure 1: (a) Digital image of the synthesised BTFMO-PVA nanocomposite film, (b) FESEM image of the pristine PVA, (c) FESEM image of the film sample (inset shows the cros-sectional view).

given in Figure 1 (c). It is observed that the nanocomposite displays a homogeneous and smooth surface morphology quite similar to the pristine PVA film [Figure 1 (b)]. Only the nanofillers appear to be rougher and containg bigger grains out of the PVA matrix. It can be also demonstrated that the nanocomposite possesses a good degree of dispersion of the nanofiller. The overall surface roughness is very low showing crack/kink free smooth surface.

Figure 2 (a) presents the Arrhenius fittings of the temperature dependence of AC electrical conductivity [log of (σ_{ac}) versus 1000/T at different frequencies (500 KHz, 800 KHz, 1M Hz, 1.5 MHz, & 2 MHz). These plots show that at lower temperatures, electrical conductivity increases with increasing frequency. In PVA, dielectric α-transition occurs as the existing flexible polar groups rotate with

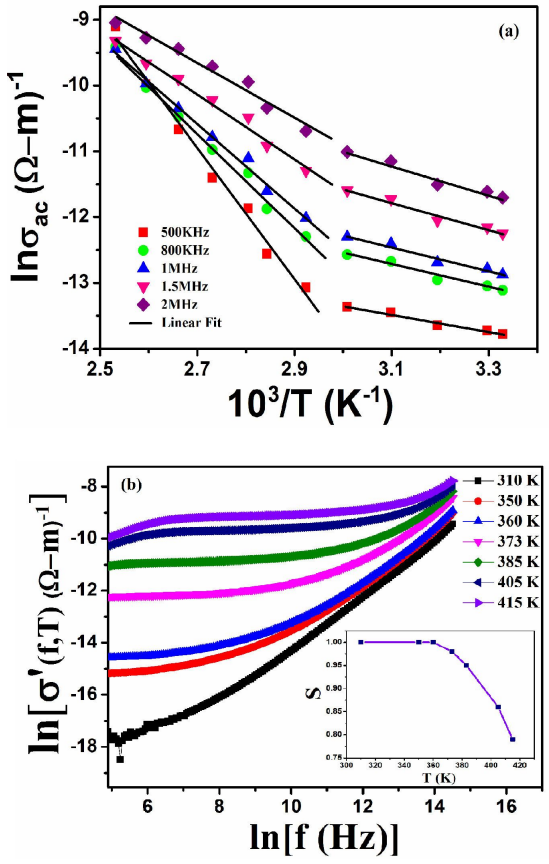

Figure 2: (a) AC conductivity variation with temperature of the sample, (b) Frequency variation of AC conductivity (inset shows temperature variation of '*S*').

frequency. From the literature survey, it is observed that dielectric behaviour of PVA undergoes α-relaxation process at ~ 360 K. The dielectric α-transition associates with the glass transition temperature, T_g. In the present investigated film sample, the glass transition temperature (T_g) is found to be around 348 K. Here, micro-Brownian motion along the main chain in the amorphous regions and the segmental motion within the crystalline phase of PVA nanocomposite occur [10, 11]. Due to the change in the chemical composition and the formation of charge-transfer-complexes (CTCs) in PVA chains, the electrical conductivity enhances [12]. As the temperature rises, the conductivity dispersion region is reduced. The temperature dependence of σ_{ac} is stronger at low frequencies than at relatively higher frequencies. This suggests that the conductivity is a thermally activated charge transport process from different localised states. This properties of a material is governed by Arrhenius equation as follows,

$$\sigma_{ac}(f, T) = \sigma_0 \exp\left[-\left(\frac{E_A}{k_B T}\right)\right], \quad (1)$$

where σ_0 is a conductivity exponential factor, E_A is the AC activation energy for mobile ions, and k_B is the Boltzmann's constant. The activation energy values are listed in Table 1. The existence of multiple activation energies from each curve indicates different current conduction mechanisms inside the sample. Multiple activation energies for the conduction and the relaxation may be due to the fact that the relaxation process involves only the hopping energy of the carriers between the localised states, but the conduction mechanism involves the hopping energy as well as the disorder and binding energy of polarons [13]. At lower temperature regions, the activation energy decreases with the increase in frequency. Lower values of the obtained activation energy confirm the applicability of hopping conduction mechanism in the nanocomposite system [14].

Further, we have studied the variation of total measured conductivity with frequency. The total conductivity obeys Jonscher's power law named as Universal Dielectric Response (UDR) as follows [15, 16],

$$\sigma'(f) = \sigma_{dc} + \sigma_{ac}(f) = \sigma_{dc} + \alpha f^S, \quad (2)$$

where σ_{dc} is the DC conductivity, α is a temperature-dependent constant which depends on the intrinsic properties of a material, and S is a power law exponent. S represents the measure of correlation between the nanofiller particles and the polymer matrix. For UDR, $S \leq 1$. The values of S are ascertained from the linear variation of $\ln \sigma'(f, T)$ vs. $\ln f$ plot [shown in Figure 2 (b)]. With increasing temperature, frequency independent behaviour is found to be dominant. At higher frequency, long range movement of mobile charge carriers is dominant. The deviation from σ_{ac} value in low frequency region is due to the electrode polarisation. The dispersion of σ_{ac} at lower temperature possibly suggests the accumulation of space charge in the material and it vanishes at higher temperature and frequency. The value of σ_{dc} increases with the increase in temperature because the thermally activated drift mobility of ions increases according to the hopping conduction mechanism. The values of '*S*' as a function is shown in the inset of Figure 2 (b). Different models have been proposed to explain the conduction mechanism on the basis of the parameter S. If S is temperature independent, quantum mechanical tunnelling (QMT) model is expected. If S increases with temperature, then small polaron hopping (SPH) model is predominant. If S initially decreases with temperature reaching a minimum value and then increases, then the overlapping large-polaron (OLP) model is the most probable mechanism. Here S is independent of frequency but decreases as the temperature increases [17]. This result reveals that correlated barrier

Table 1: Derived electrical parameter (activation energy) from Arrhenius plot.

Derived electrical parameter	500 kHz	800 kHz	1 MHz	1.5 MHz	2 MHz
E_A (eV) at high temperature region	0.11	0.15	0.16	0.18	0.19
E_A (eV) at low temperature region	0.86	0.62	0.55	0.43	0.36

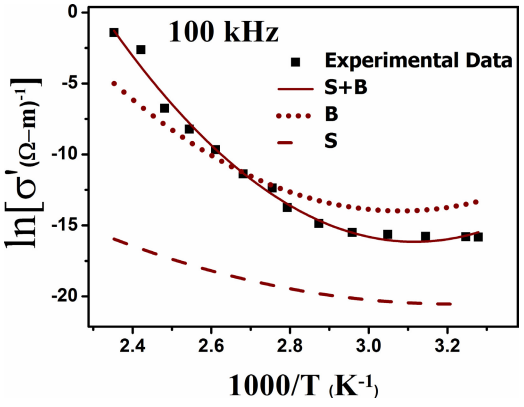

Figure 3: Plot of ln σ vs. 1000/T for the film sample at 100 kHz frequency.

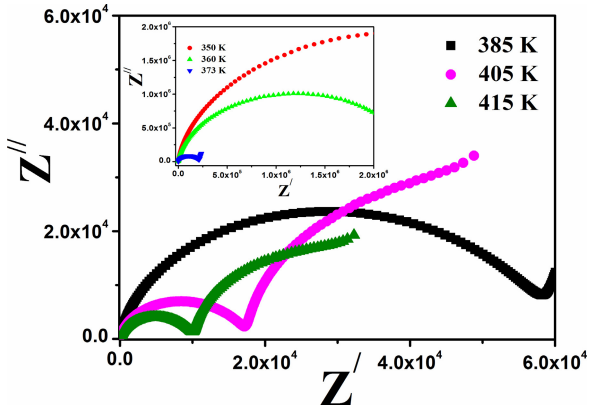

Figure 4: Impedance spectra of the film at higher temperatures (inset shows Impedance spectra of the sample at lower temperatures).

hopping (CBH) conduction model is the most suitable representation to characterise the electrical conduction [18]. In this model, conduction of carriers takes place through the hopping between the localised states separating by barrier. In CBH model also, two kind of conduction can occur between two defect sites (D^+ and D^-): 1. single polaron hopping and 2. bipolaron hopping. The ac conductivity can be expressed as follows,

$$\sigma_{ac}(\omega) = n\pi^3 \varepsilon\varepsilon_0 N N_P \omega (R_\omega)^6/6, \tag{3}$$

where N is the density of localised states where carriers exist, N_P is the density of localised states to which carriers hop, $n = 2$ and $n = 1$ for bipolaron and single polaron hopping, R_ω is the hopping distance [19]. Figure 3 shows the plots of the contributions for single polaron (S) and bipolaron (B) hopping processes and their sum (S+B) by fitting the above Eq. 3 with the experimental data of conductivity at 100 kHz frequency. It is clear from the figure that single polaron hopping contribution is much smaller and hence the conduction mechanism mostly occurs via bipolaron hopping.

The complex admittance spectroscopy is very important tool to understand the interfacial charge carrier motion in the interlayer of electrode-semiconductor material [20]. Total AC electrical data acquired in the form of the admittance over frequency range 20 Hz – 2 MHz are used to represent the best meaning of the dispersion. Figure 4 (a) – (b) show the frequency dependent real part (Y') and the imaginary part (Y'') of complex admittance of the film at different experimental temperatures. The admittance measurements show the evidence of a narrow distribution of trap states near the BTFMO-PVA interface. The peak structure in the frequency dependent imaginary admittance (Y'') plot arises due to the defect states/traps at the barrier interface of the nanocomposite [21].

The effective dielectric response in an inhomogeneous system can be further explained by Complex impedance spectroscopy. This study offers an insight of the electrical processes taking place within the system and their correlation with the sample when modelled in terms of its equivalent circuit. This observation is capable to to study the electrical properties like grain resistance (R_g), grain boundary resistance (R_{gb}) and electrode interface under the influence of applied frequency range [22]. The expression of the complex impedence is given as follows [23],

$$Z' = \frac{R_g}{1 + (\omega_g R_g C_g)^2} + \frac{R_{gb}}{1 + (\omega_{gb} R_{gb} C_{gb})^2} \tag{4}$$

$$Z'' = \frac{\omega_g {R_g}^2 C_g}{1 + (\omega_g R_g C_g)^2} + \frac{\omega_{gb} {R_{gb}}^2 C_{gb}}{1 + (\omega_{gb} R_{gb} C_{gb})^2}, \tag{5}$$

Where R_g and are the grain resistance and grain boundary resistance respectively. C_g and C_{gb} are the grain capacitance and grain boundary capacitance respectively. ω_g and ω_{gb} are the angular frequencies at the peak of the grain and grain boundary semicircles respectively. Maxwell-Wagner capacitor model is taken here to under-

Table 2: Derived electrical parameters (grain resistance, grain boundary resistance, grain capacitance, grain boundary capacitance, grain relaxation time, grain boundary relaxation time) from Nyquist plot.

Derived Parameters	R_g (Ω)	C_g (pF)	τ_g (ms)	R_{gb} (Ω)	C_{gb} (pF)	τ_{gb} (ms)
350 K	4.46×10^{6}	100.94	0.45	–	–	–
360 K	2.55×10^{6}	104.58	0.27	–	–	–
373 K	7.10×10^{5}	38.93×10^{3}	18.24	2.40×10^{5}	126.11	0.028
385 K	2.93×10^{5}	31.95×10^{3}	9.17	5.99×10^{4}	132.11	7.93×10^{-3}
405 K	9.21×10^{4}	12.25×10^{3}	7.52	1.77×10^{4}	133.81	2.37×10^{-3}
415 K	5.24×10^{4}	8.28×10^{3}	6.33	1.02×10^{4}	138.30	1.42×10^{-3}

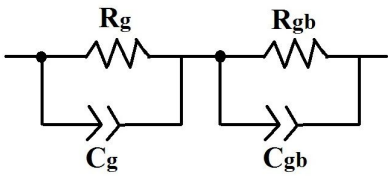

Figure 5: The equivalent circuit diagram (R-C circuit) for the Impedance spectra.

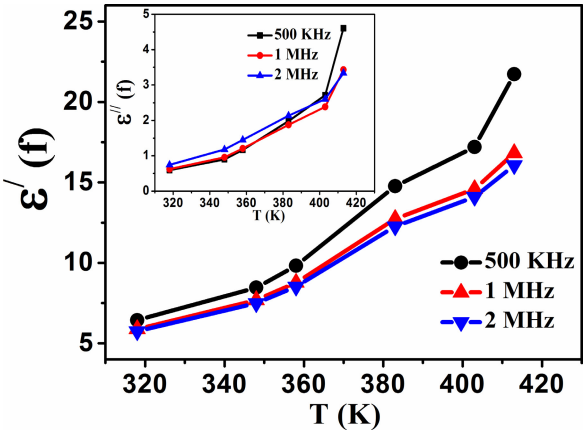

Figure 6: The temperature variation of real part (ε') of dielectric constant of the sample at different frequencies (inset shows the temperature variation of imaginary part (ε'') of dielectric constant at different frequencies).

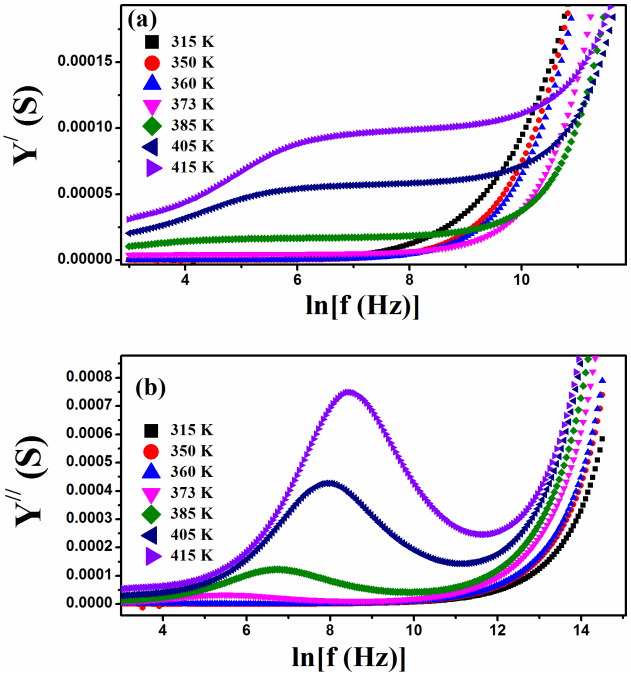

Figure 7: (a) The frequency dependence of real part (Y') of Admittance of the sample at different temperatures, (b) Frequency dependence of imaginary part (Y'') of Admittance of the sample at different temperatures.

stand the complex impedance of the sample. Nyquist plots (imaginary impedance $[Z''(f)]$ vs. real impedance $[Z'(f)]$) of the film sample at selective temperatures are shown in Figure 5. The equivalent electrical circuit (parallel R-C circuit) model diagram is shown in Figure 6 that is fitted with the experimental data to evaluate the parameters (listed in Table 2). The plots exhibit semicircular arc in the high frequencies. A semicircular arc having a trend to form two semicircular arcs tells about both grain and grain boundary contribution to the electric conductivity. At low temperatures (350 K and 360 K), the plot consists of one region over the whole frequency range *i.e.* the grain effect only. Here semicircle with the center lying below the real axis exhibits non-Debe type behavior [24]. Furthermore, the relxation time for grain and grain boundary can be expressed using the relations, and $\tau_{gb} = 1/\omega_{gb}$ and the calculated values of relaxation time are listed in Table 2.

The temperature variation of the real part $[\varepsilon'(f)]$ and the imaginary part $[\varepsilon''(f)]$ of the dielectric constant at different frequencies are shown in Figure 7. At a particular frequency, the value of the dielectric constant increases thoroughly with temperature. Further, the temperature variation of the dielectric constant is more prominent in lower frequency than that of higher one. At high frequency, dipoles get opposed in orienting themselves along

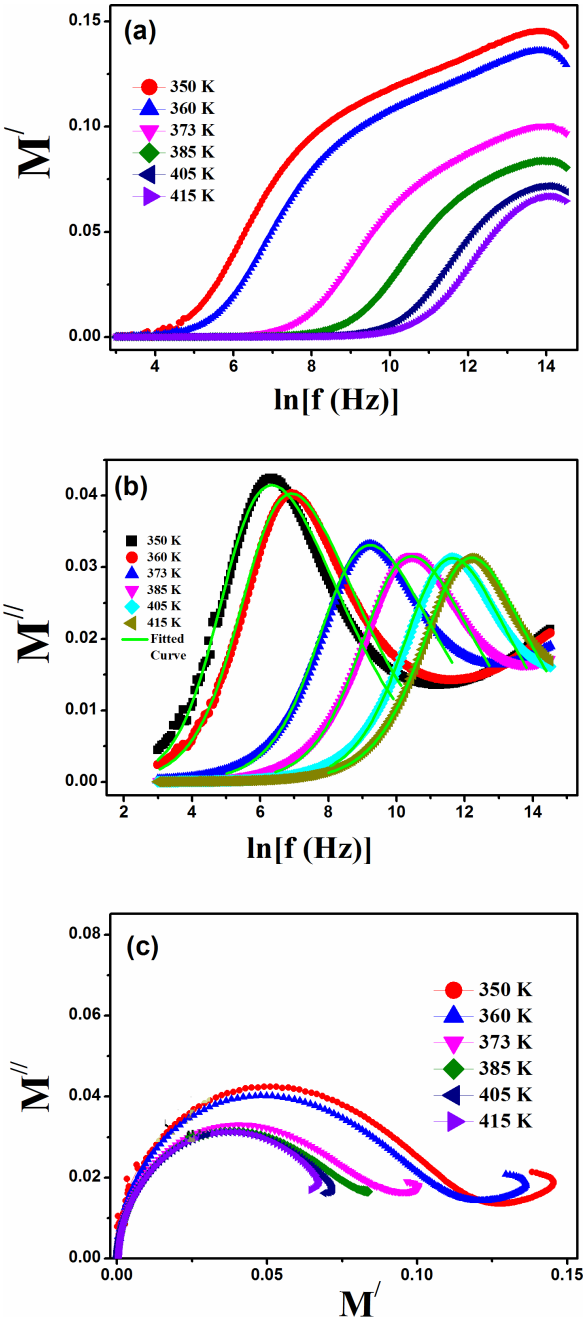

Figure 8: (a) Real electric modulus (M') spectra of the sample, (b) electric modulus (M'') spectra of the sample, (c) Complex electric modulus spectra in the electric modulus plane.

the applied field. For the mutual movement of dipoles and charges, an electric relaxation arises. The dielectric relaxation behaviour is the result of the combination of two polarisation mechanisms (interfacial polarisation and space charge polarisation) that depend on the physical movement of the charges responsible for the dipoles and on the length of time required for the displacement [25].

Electric modulus spectroscopy is studied to understand the space charge relaxation behavior in the sample.The real part $[M']$ and the imaginary part $[M'']$ of complex electric modulus spectra of the sample are shown in Figure 8 (a) - (b), respectively. M' goes to zero at lower frequencies due to the absence of electrode polarization. With the increase in frequency, the spectra show a step function dependence on frequency. This type of behavior gives rise to the well-defined loss peak in the M'' spectra. With increasing temperature, the peaks appear to shift systematically towards higher frequency. These spectra tell about two apparent relaxation zones. The peak shift exhibit the thermally activated nature of relaxation time. The left side of the asymmetric peak indicates the conduction mechanism of charge carriers over a long-range while the right portion corresponds to the charges confined to a potential well [26]. Modified Kohlrausch-Williams-Watts (KWW) function is required here to account for the asymetric distribution of the characteristic peak. The imaginary electric modulus can be formulated as follows [27],

$$M''(f) = \frac{M''_{\max}}{\frac{(1-|a-b|)}{a+b}\left[b\left(\frac{f}{f_{\max}}\right)^{-a} + a\left(\frac{f}{f_{\max}}\right)^{b}\right] + |a-b|}, \quad (6)$$

where 'a' and 'b' are shape parameters describing the symmetric and asymmetric broadening of the relaxation curve and their obtained values are given in Table 3.

To avoid the ambiguity arising out of the presence of grain or grain boundary effect at different temperatures, the impedance data are plotted in the complex modulus plane. Further, the modulus spectra [Figure 8 (c)] show a change in its size and shape with the rise in temperature. It suggests a probable change in the values of capacitance as a function of temperature. The semicircular arc indicates the conductivity relaxation [28]. The plot has a tendency of two deformed semicircles indicating the occurance of both grain and grain boundary contributions in the nanocomposite film. The centre of the circles lying below the ordinate. It indicates non-Debye type relaxation of the sample.

Figure 9 shows the variation of magnetocapacitance with the applied magnetic field at different frequencies (20 kHz and 50 kHz) at room temperature. Magnetocapacitance is stated as follows [29],

$$MC(\%) = \frac{\varepsilon'(H) - \varepsilon'(0)}{\varepsilon'(0)} \times 100, \quad (7)$$

where $\varepsilon'(H)$ and $\varepsilon'(0)$ are the dielectric constants at the magnetic field H and zero, respectively. The plot shows the negative magnetocapacitance effect of the sample. The magnetocapacitance value increases with the increase in the applied magnetic field. Maxwell-Wagner type polarisa-

Table 3: Derived electrical parameters (shape parameters) from from electrical modulus spectra analysis.

Derived electrical parameters	350 K	360 K	373 K	385 K	405 K	415 K
a	0.99	0.98	0.97	0.95	0.95	0.93
b	0.65	0.60	0.57	0.56	0.47	0.46

Table 4: Junction barrier height, dynamic dielectric constant of the sample from current-voltage characteristics study.

Derived electrical parameters	300 K	330 K	365 K	385 K	405 K
φ_B (eV)	2.24	1.96	1.39	1.04	0.83
ε_r	0.67	0.42	0.21	0.18	0.12

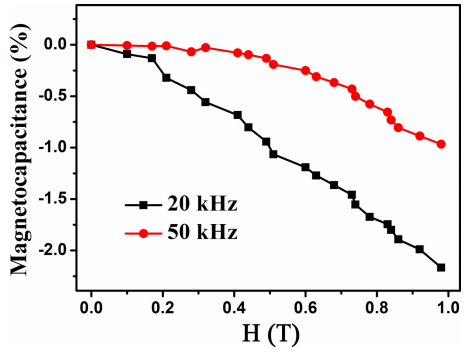

Figure 9: Magnetocapacitance of the sample with the applied magnetic field at rom temperature at selective frequencies.

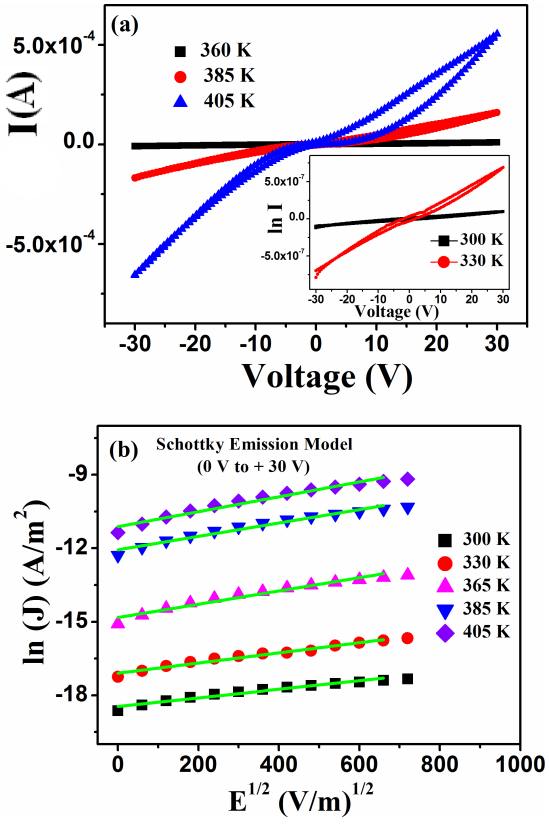

Figure 10: (a) I vs. V curves of the sample at different temperatures, (b) ln J vs. $E^{1/2}$ plots at different temperatures.

tion in the sample is the responsible factor for this type of behavior.

Figure 10 (a) shows the non-linearity of current-voltage (I-V) characteristics curve at different experimental temperatures within the applied voltage range ± 30 V. It shows good rectifying property of the sample. The curves display strong temperature dependence behavior. The Schottky Emission (SE) model can explain the current conduction mechanism in the nanocomposite system. According to this model, thermally activated electrons gain sufficient energy to overcome a potential barrier at the electrode-semiconductor interface to produce current [30]. Current density can be written as,

$$J_{SE} = A^{\star} T^2 \exp\left[-\frac{q\varphi_B - \sqrt{\frac{q^3 E}{4\pi\varepsilon_0\varepsilon_r}}}{k_B T}\right], \qquad (8)$$

where $A^{\star}$ is a constant, φ_B is the zero-field junction barrier height, q is electronic charge, ε_0 and ε_r are the free space dielectric constant and dynamic dielectric constant respectively. In Figure 10 (b), ln J vs. $E^{1/2}$ plot of I-V experimental data of the sample is shown at different experimental temperatures. Extracted values of φ_B and ε_r are given in Table 4. Both the values of Schottky barrier height and optical dielectric constant decrease with increasing temperature.

4 Conclusion

We report a detailed investigation on the charge conduction mechanism in BTFMO-PVA nanocomposite film system. The existence of multiple activation energies implies different current conduction mechanisms at different tem-

perature regions. Correlated barrier hopping model explains the electrical transport mechanism through the polymeric matrix. Non-Debye type relaxation process is also observed which has been further demonstrated by the modified Kohlrausch-Williams-Watts (KWW) model. Complex impedance spectroscopy of the nanocomposite film clearly shows the grain and grain boundary contributions. Negative magnetocapacitance arises in the sample due to the Maxwell-Wagner type polarization at the interface. The film exhibits charge storage ability that may be potentially applicable in the electronic world. As the nanocomposite film responds well with temperature as well as ecternal magnetic field, this film has potential applicabilities in thermistor, magnetic field sensors.

Acknowledgement: This work is financially supported by DST-SERB (Grant No. EMR/2016/001409), Govt. of India. The authors acknowledge the Centre of Excellence, NIT Durgapur for the FESEM facility. One of the authors (MH) would like to acknowledge DST-INSPIRE for providing fellowship.

Conflict of Interests: We have no confict of interest.

References

[1] Prabhakaran, T., and J. Hemalatha. Synthesis and characterization of magnetoelectric polymer nanocomposites. *Journal of Polymer Science. Part B, Polymer Physics*, Vol. 46, No. 22, 2008, pp. 2418–2422.

[2] Mukherjee, P. S., A. K. Das, B. Dutta, and A. K. Meikap. Role of silver nanotube on conductivity, dielectric permittivity and current voltage characteristics of polyvinyl alcohol-silver nanocomposite film. *Journal of Physics and Chemistry of Solids*, Vol. 111, 2017, pp. 266–273.

[3] Dabra, N., J. S. Hundal, K. C. Sekhar, A. Nautiyal, and R. Nath. Preparation and characterization of the ferroelectric potassium nitrate: Poly(vinyl alcohol) composite films. *IEEE Transactions on Ultrasonics, Ferroelectrics, and Frequency Control*, Vol. 56, No. 8, Aug. 2009, pp. 1627–1633.

[4] Bindu, P., and S. Thomas. Estimation of lattice strain in ZnO nanoparticles: X-ray peak profile analysis. *Journal of Theoratical and Applied Physics*, Vol. 8, No. 4, 2014, pp. 123–134.

[5] Hwang, J. S., J. Y. Cho, S. Y. Park, Y. J. Yoo, P. S. Yoo, B. W. Lee, and Y. P. Lee. Multiferroic properties of stretchable $BiFeO_3$ nanocomposite film. *Applied Physics Letters*, Vol. 106, No. 6, 2015, p. 062902.

[6] Halder, M., A. K. Das, and A. K. Meikap. Effect of BiFeO3 nanoparticle on electrical, thermal and magnetic properties of polyvinyl alcohol (PVA) composite film. *Materials Research Bulletin*, Vol. 104, 2018, pp. 179–187.

[7] Hossain, S. M., A. Mukherjee, S. Basu, and M. Pal. Effect of Ni–Co codoping on structure and electrical properties of multiferroic BiFeO3 nanoparticles. *Micro & Nano Letters*, Vol. 8, No. 7, 2013, pp. 374–377.

[8] Wang, J., J. Hu, L. Yang, K. Zhu, B. W. Li, Q. Sun, Y. Li, and J. Qiu. High discharged energy density of polymer nanocomposites induced by Nd-doped BaTiO3 nanoparticles. *J Materiomics*, Vol. 4, No. 1, 2018, pp. 44–50.

[9] Halder, M., and A. K. Meikap. Electrical transport properties of Tb and Mn codoped bismuth ferrite embedded poly (vinyl alcohol) nanocomposite film. *AIP Conference Proceedings*, Vol. 2115, 2019, id. 030429.

[10] Kader, F. H. A. E., W. H. Osman, K. H. Mahmoud, and M. A. F. Basha. Dielectric investigations and ac conductivity of polyvinyl alcohol films doped with europium and terbium chloride. *Physica B, Condensed Matter*, Vol. 403, No. 19-20, 2008, pp. 3473-3484.

[11] Hanafy, T. A. Dielectric relaxation and alternating current conductivity of lanthanum, gadolinium, and erbium-polyvinyl alcohol doped films. *Journal of Applied Physics*, Vol. 112, No. 3, 2012, p. 034102.

[12] Mahendia, S., A. K. Tomar, and S. Kumar. Electrical conductivity and dielectric spectroscopic studies of PVA–Ag nanocomposite films. *Journal of Alloys and Compounds*, Vol. 508, No. 2, 2010, pp. 406–411.

[13] Imran, Z., M. A. Rafiq, M. Ahmad, K. Rasool, S. S. Batool, and M. M. Hasan. Temperature dependent transport and dielectric properties of cadmium titanate nanofiber mats. *AIP Advances*, Vol. 3, No. 3, 2013, p. 032146.

[14] Nahass, M. M. E., and H. A. M. Ali. AC conductivity and dielectric behavior of bulk Furfurylidenemalononitrile. *Solid State Communications*, Vol. 152, No. 12, 2012, pp. 1084-1088.

[15] Das, S. N., A. Pattanaik, S. Kadambini, S. Pradhan, S. Bhuyan, and R. N. P. Choudhary. Dielectric and impedance spectroscopy of Ni doped BiFeO3-BaTiO3 electronic system. *Journal of Materials Science Materials in Electronics*, Vol. 27, No. 10, 2016, pp. 10099–10105.

[16] Jonscher, A. K. The 'universal' dielectric response. *Nature*, Vol. 267, No. 5613, 1977, pp. 673–679.

[17] Joshi, J. H., G. M. Joshi, M. J. Joshi, and K. D. Parikh. Complex impedance, FT-Raman, and photoluminescence spectroscopic studies of pure and L-phenylalanine doped ammonium dihydrogen phosphate single crystals: The correlation with hydrogen bonding defect. *Ionics*, Vol. 25, No. 7, 2019, pp. 3223–3245.

[18] Elliot, S. R. A.c. conduction in amorphous chalcogenide and pnictide semiconductors. *Advances in Physics*, Vol. 36, 1987, pp. 135-217.

[19] Shimakawa, K. Contribution of Single Polaron Hopping to Ac Conduction in Amorphous Chalcogenides. *Journal de Physique Colloques*, Vol. 42, No. C4, 1981, pp. C4-167-C4-170.

[20] Joshi, J. H., S. Kalainathan, M. J. Joshi, and K. D. Parikh. Effect of l-threonine on growth and properties of ammonium dihydrogen phosphate crystal. *Arabian Journal of Chemistry*, Vol. 13, No. 1, 2020, pp. 1532–1550.

[21] Heath, J. T., J. D. Cohen, and W. N. Shafarman. Bulk and metastable defects in CuIn1-xGaxSe2 thin films using drive-level capacitance profiling. *Journal of Applied Physics*, Vol. 95, No. 3, 2004, pp. 1000–1010.

[22] Joshi, J. H., D. K. Kanchan, M. J. Joshi, H. O. Jethva, and K. D. Parikh. Dielectric relaxation, complex impedance and modulus spectroscopic studies of mix phase rod like cobalt sulfide nanoparticles. *Materials Research Bulletin*, Vol. 93, 2017, pp. 63–73.

[23] Joshi, J. H., G. M. Joshi, M. J. Joshi, H. O. Jethva, and K. D. Parikh. Raman, photoluminescence, and a.c. electrical studies of pure and l -serine doped ammonium dihydrogen phosphate single crystals: An understanding of defect chemistry in hydrogen bonding. *New Journal of Chemistry*, Vol. 42, No. 21, 2018, pp. 17227–17249.

[24] Patri, S. K., P. L. Deepti, R. N. P. Choudhary, and B. Behera. Dielectric, impedance and modulus spectroscopy of BaBi2Nb2O9. *Journal of Electroceramics*, Vol. 40, No. 4, 2018, pp. 338–346.

[25] Ashery, A., A. H. Zaki, M. H. Mourad, A. M. Azab, and A. A. M. Farag. Structural and frequency dependencies of a.c. and dielectric characterizations of epitaxial InSb-based heterojunctions. *Bulletin of Materials Science*, Vol. 39, No. 4, 2016, pp. 1057–1063.

[26] Joshi, J. H., D. K. Kanchan, H. O. Jethva, M. J. Joshi, and K. D. Parikh. Dielectric relaxation, protonic defect, conductivity mechanisms, complex impedance and modulus spectroscopic studies of pure and L-threonine-doped ammonium dihydrogen phosphate. *Ionics*, Vol. 24, No. 7, 2018, pp. 1995–2016.

[27] Macedo, P. B., C. T.Moynihan, and R. Bose. The Role of Ionic Diffusion in Polarization in Vitreous Ionic Conductors. *Physics and Chemistry of Glasses*, Vol. 13, 1972, pp. 171–179

[28] Mrudula, M. S., and M. R. G. Nair. Dielectric properties of natural rubber/polyethylene oxide block copolymer complexed with transition metal ions. *Polymer Bulletin*, 2019. DOI: https://doi.org/10.1007/s00289-019-03035-z

[29] Tang, R., H. Zhou, W. You, and H. Yang. Room-temperature multiferroic and magnetocapacitance effects in M-type hexaferrite $BaFe_{10.2}Sc_{1.8}O_{19}$. *Applied Physics Letters*, Vol. 109, No. 8, 2016, p. 082903.

[30] Jung, K., Y. Kim, H. Im, H. Kim, and B. Park. Leakage transport in the high-resistance state of a resistive-switching NbOx thin film prepared by pulsed laser deposition. *Journal of the Korean Physical Society*, Vol. 59, No. 4, 2011, pp. 2778–2781.